This paper appears in Intelligent Service Robotics, 2026.
DOI: 10.1007/s11370-026-00700-x

Variable Admittance Control for Door Opening with a Wheeled Mobile Manipulator Considering Ground Obstacles

Hongjun Xing[1*], Yanqing Liu[1], Jinbao Chen[1], Weihua Li[2*], Liang Ding[3], Mahdi Tavakoli[4]

[1]National Key Laboratory of Aerospace Mechanism, Nanjing University of Aeronautics and Astronautics, Nanjing 210016, China.
[2]School of Automotive Engineering, Harbin Institute of Technology (Weihai), Weihai 264209, China.
[3]State Key Laboratory of Robotics and System, Harbin Institute of Technology, Harbin 150001, China.
[4]Department of Electrical and Computer Engineering, University of Alberta, Edmonton T6G 1H9, Alberta, Canada.

*Corresponding author(s). E-mail(s): xinghj@nuaa.edu.cn; liweihua@hit.edu.cn;

Abstract

Robotic operations such as opening doors in complex environments pose challenges due to unmodeled constraints and unknown interactions. This paper proposes a variable admittance control approach with both positional and orientational compliance for a wheeled mobile manipulator (WMM) to perform door-opening tasks while avoiding ground obstacles. The controller adaptively adjusts its parameters based on real-time motion states and estimated interaction forces and torques. Redundancy in the system enables simultaneous dual-trajectory tracking for the mobile base and the end-effector. A Lyapunov-based stability analysis guarantees system stability, and dedicated force/torque estimation experiments validate the interaction measurements. The method is implemented on an omnidirectional WMM performing a door-opening task with an obstacle in the base's path. Experimental results demonstrate safe and compliant interaction, accurate trajectory tracking, and successful obstacle avoidance.

Keywords: Door opening, Wheeled mobile manipulator, Variable admittance control, Full pose compliance, Dual-trajectory tracking.

1 Introduction

Robotic applications in complex environments, including mobile manipulation, require significantly higher performance than simple or repetitive tasks. Wheeled mobile manipulators (WMMs) integrate the high mobility of a mobile base (MB) with the dexterity of a manipulator, enabling human-like operations such as opening doors in obstacle-rich environments [1, 2]. Unlike humans, who naturally adjust their applied forces while coordinating body movements to avoid obstacles, WMMs lack innate perception and adaptive force control, making door-opening a challenging task. Sophisticated motion planning and compliance control strategies are essential to achieve human-like interaction.

Door-opening is a crucial capability for mobile manipulators deployed in real-world applications, including search-and-rescue missions, hazardous site exploration, and assistive robotics in healthcare environments [3–5]. In disaster response, robots must navigate closed or obstructed doors to access affected areas, while assistive robots in hospitals and elderly care facilities must reliably open doors despite environmental uncertainties. However, traditional fixed-compliance controllers struggle with variable resistance and unexpected disturbances, necessitating adaptive compliance control methods.

The primary challenge in door-opening tasks lies in the kinematic constraints imposed on the WMM while gripping and manipulating the door [6]. Given the rigidity of the WMM's hardware, even slight motion deviations can induce excessive interaction forces, risking failure in both manipulation and locomotion. To address this, researchers have explored various door parameter estimation methods, such as geometric parameter estimation through coordinate transformation [7], constraint estimation via force/torque measurements [8], and vision- and LiDAR-based parameter identification [9, 10]. However, none of these methods guarantee precise parameter estimation, making compliance control a critical factor in ensuring successful door-opening execution.

The compliance control approach is instrumental in enabling robots and their environments to interact in a compliant manner. Two fundamental methods in this domain are hybrid position/force control [11] and impedance control [12, 13]. Impedance and admittance control represent two ways of implementing impedance control, differentiated by the causality of the controller [14]. Compared to impedance control, admittance control offers the advantage of compatibility with modern industrial systems, specifically position-control and velocity-control systems [15, 16]. Xing *et al.*[17] introduced an admittance control method for WMMs to facilitate human-robot interaction, though it used fixed parameters. Tu *et al.*[18] proposed a variable admittance control approach to enhance compliance in human-exoskeleton interactions, where parameters adjust based on deviations between actual and standard interaction forces.

Ding *et al.*[19] presented a variable admittance control method for WMMs to detect users' walking intentions for mobility assistance. Additionally, several tank-based approaches have been proposed for admittance controllers to ensure compliance control system stability [20–22].

Achieving compliant contact between the WMM's end-effector (EE) and the door alone is insufficient for door-opening operations in environments with obstacles; obstacle avoidance for the MB must also be addressed. This challenge can be managed by leveraging the redundancy characteristics of the WMM. However, solving the inverse kinematics for redundant manipulators is challenging due to the presence of more unknowns than equations. Currently, two main methods address this problem: the null-space-based approach [1, 23] and the quadratic programming approach [24, 25]. Wang *et al.* [26] proposed an online obstacle avoidance strategy based on quadratic programming for a nonholonomic WMM, including dual-trajectory generation for the MB and EE. Xing *et al.* [27] designed a task-priority-based dual-user teleoperation framework for a WMM to perform tasks in constrained environments, enabling simultaneous manipulation of the MB and the EE. Mashali *et al.* [28] presented a task-priority-based dual-trajectory control for redundant WMMs, though it did not consider orientation control.

Existing research on door-opening tasks with WMMs has primarily focused on identifying the kinematic constraints of the target door [7] or achieving position compliance between the EE and the door [29]. However, relatively little attention has been given to orientation compliance during the door-opening process or to potential motion interference from ground obstacles. Although some dual-trajectory tracking approaches have been proposed for redundant WMMs [26, 27], these lack consideration for compliant interaction requirements during motion. A practical door-opening framework that accounts for ground obstacles remains an open area of research.

This study proposes a unified control framework for compliant manipulation in constrained environments, which couples variable admittance control with task-priority-based redundancy resolution. After obtaining the target door's motion parameters and the positions of ground obstacles, the proposed method employs a dual-level admittance control to achieve full-pose compliance of the EE while dynamically adjusting the compliance parameters according to real-time motion states and interaction forces. Simultaneously, a null-space-based dual-trajectory tracking scheme coordinates the redundant motion of the MB and EE to avoid ground obstacles without disturbing the primary manipulation task.

This research seeks to address three key questions: (a) How can variable admittance control enable compliant interaction under unpredictable resistance? (b) How can task-priority-based dual-trajectory tracking improve coordination between the EE and MB to handle conflicting motion objectives? (c) Can integrating variable admittance control with redundancy-based dual-trajectory tracking effectively reduce interaction forces compared to fixed admittance methods?

The main contributions of this work are as follows: (1) A unified control framework is established that seamlessly couples variable admittance control with both positional and orientational compliance and task-priority-based redundancy resolution, enabling simultaneous compliant interaction and obstacle-avoidance behavior; (2) A

variable admittance controller with real-time adaptive stiffness and damping adjustment is developed to regulate EE position and orientation, while a task-priority-based dual-trajectory tracking scheme allows the redundant WMM to coordinate MB and EE motions through null-space projection without mutual interference; (3) Lyapunov-based stability analysis is provided to rigorously guarantee the stability of the proposed variable admittance control system under time-varying parameters. Although validated on a door-opening task, the proposed framework is general and can be extended to other contact-rich manipulation scenarios such as valve turning, drawer opening, and human–robot co-manipulation.

The rest of this paper is structured as follows. Section 2 introduces the kinematics of WMMs and the proposed dual-trajectory tracking method. Section 3 presents a variable admittance controller that accounts for both position and orientation compliance. Experimental validations and performance evaluations of the proposed method are provided in Section 4. Finally, Section 5 concludes the paper.

2 Kinematics and Dual-trajectory Tracking of WMMs

This section presents the forward kinematics at the velocity level for WMMs and introduces a task-priority-based dual-trajectory tracking approach, enabling simultaneous planning and tracking of trajectories for the manipulator's EE and the MB.

2.1 Kinematics of WMMs

The kinematic model of a MB, assuming no slippage or skidding, is expressed as $\dot{\boldsymbol{q}}_b = \boldsymbol{G}(\boldsymbol{q}_b)\boldsymbol{v}_b$, where $\dot{\boldsymbol{q}}_b \in \mathbb{R}^{n_b}$ denotes the generalized coordinate vector of the MB, and $\boldsymbol{v}_b \in \mathbb{R}^b$ is the input velocity vector of the wheels [30]. The matrix $\boldsymbol{G}(\boldsymbol{q}_b) \in \mathbb{R}^{n_b \times b}$ represents the MB's constraint matrix, which may be holonomic or nonholonomic. The generalized velocity vector of the manipulator, $\dot{\boldsymbol{q}}_m \in \mathbb{R}^m$, can be freely assigned based on the manipulator's configuration. Specifically, $\dot{\boldsymbol{q}}_m = \boldsymbol{v}_m$, where $\boldsymbol{v}_m \in \mathbb{R}^m$ represents the joint velocity input vector for the manipulator.

The generalized coordinate vector and velocity input vector for the WMM are defined as $\boldsymbol{q} = [\boldsymbol{q}_b^{\mathrm{T}}, \boldsymbol{q}_m^{\mathrm{T}}]^{\mathrm{T}} \in \mathbb{R}^{n_b+m}$ and $\boldsymbol{v} = [\boldsymbol{v}_b^{\mathrm{T}}, \boldsymbol{v}_m^{\mathrm{T}}]^{\mathrm{T}} \in \mathbb{R}^n$, respectively, where $n = b + m$. The forward kinematics of a WMM at the velocity level can then be computed as:

$$\begin{aligned} \dot{\boldsymbol{x}}_e &= \boldsymbol{J}_q(\boldsymbol{q})\dot{\boldsymbol{q}} = [\boldsymbol{J}_b(\boldsymbol{q}), \boldsymbol{J}_m(\boldsymbol{q})] \begin{bmatrix} \dot{\boldsymbol{q}}_b \\ \dot{\boldsymbol{q}}_m \end{bmatrix} \\ &= [\boldsymbol{J}_b(\boldsymbol{q})\boldsymbol{G}(\boldsymbol{q}_b), \boldsymbol{J}_m(\boldsymbol{q})] \begin{bmatrix} \boldsymbol{v}_b \\ \boldsymbol{v}_m \end{bmatrix} = \boldsymbol{J}(\boldsymbol{q})\boldsymbol{v}, \end{aligned} \tag{1}$$

where $\dot{\boldsymbol{x}}_e \in \mathbb{R}^{n_1}$ denotes the task-space velocity vector of the EE in the world frame $\{\Sigma_w\}$, with n_1 representing its dimension. The matrices $\boldsymbol{J}_b(\boldsymbol{q}) \in \mathbb{R}^{n_1 \times n_b}$ and $\boldsymbol{J}_m(\boldsymbol{q}) \in \mathbb{R}^{n_1 \times m}$ are the Jacobians of the MB and the manipulator, respectively.

$\boldsymbol{J}_q(\boldsymbol{q}) \in \mathbb{R}^{n_1 \times n}$ represents the Jacobian of the generalized WMM (i.e., without considering the constraints of the MB), while $\boldsymbol{J}(\boldsymbol{q}) \in \mathbb{R}^{n_1 \times n}$ denotes the Jacobian of the constrained WMM.

Then, with the WMM velocity vector defined as $\boldsymbol{v}$, the redundancy resolution for the WMM expressed in (1) can be derived as:

$$\boldsymbol{v} = \boldsymbol{J}^{\dagger}\dot{\boldsymbol{x}}_e + \boldsymbol{\mathcal{N}}\boldsymbol{\mu}, \tag{2}$$

where $\boldsymbol{J}^{\dagger}$ denotes the pseudoinverse of Jacobian $\boldsymbol{J}$, $\boldsymbol{\mathcal{N}} = \boldsymbol{I} - \boldsymbol{J}^{\dagger}\boldsymbol{J}$ denotes the orthogonal projection operator into $\mathcal{N}(\boldsymbol{J})$, and $\boldsymbol{\mu}$ represents the user-defined joint velocity vector for any secondary task.

2.2 Dual-trajectory Tracking Controller

To achieve dual-trajectory tracking of the manipulator's EE and the MB while minimizing the impact of base motion on the EE, we introduce a redundancy resolution method incorporating task prioritization. Combining (1), the forward kinematics mapping of the MB can be computed as:

$$\dot{\boldsymbol{x}}_b = \boldsymbol{G}_b(\boldsymbol{q}_b)\boldsymbol{v}_b = \boldsymbol{J}_b(\boldsymbol{q}_b)\boldsymbol{v}, \tag{3}$$

where $\dot{\boldsymbol{x}}_b \in \mathbb{R}^{n_2}$ denotes the MB's velocity vector with n_2 being its Cartesian-space dimension, $\boldsymbol{G}_b \in \mathbb{R}^{n_2 \times b}$ represents the Jacobian of the MB related to its velocity vector, and $\boldsymbol{J}_b = [\boldsymbol{G}_b, \boldsymbol{0}_{n_2 \times m}] \in \mathbb{R}^{n_2 \times n}$ is the extended Jacobian of the MP for the following controller design.

Combining (2) and (3), we can derive:

$$\boldsymbol{v} = \boldsymbol{J}^{\dagger}\dot{\boldsymbol{x}}_e + \boldsymbol{\mathcal{N}}\boldsymbol{\mu}, \tag{4a}$$

$$\dot{\boldsymbol{x}}_b = \boldsymbol{J}_b\boldsymbol{v} = \boldsymbol{J}_b\boldsymbol{J}^{\dagger}\dot{\boldsymbol{x}}_e + \boldsymbol{J}_b\boldsymbol{\mathcal{N}}\boldsymbol{\mu}. \tag{4b}$$

According to (4b), the auxiliary variable $\boldsymbol{\mu}$ is defined as:

$$\boldsymbol{\mu} = (\boldsymbol{J}_b\boldsymbol{\mathcal{N}})^{\mathrm{T}}\left[(\boldsymbol{J}_b\boldsymbol{\mathcal{N}})(\boldsymbol{J}_b\boldsymbol{\mathcal{N}})^{\mathrm{T}} + \lambda^2\boldsymbol{I}\right]^{-1}\left(\dot{\boldsymbol{x}}_b - \boldsymbol{J}_b\boldsymbol{J}^{\dagger}\dot{\boldsymbol{x}}_e\right), \tag{5}$$

where λ is an adaptively activated damping factor used in the damped least-squares (DLS) pseudoinverse to handle algorithmic singularities [27]. Specifically, λ is set to a small positive value only when $\boldsymbol{J}_b\boldsymbol{\mathcal{N}}$ approaches rank deficiency (*i.e.*, its smallest singular value falls below a predefined threshold); otherwise, λ is set to zero, and (5) reduces exactly to the standard pseudoinverse. This conditional damping strategy ensures numerical stability near algorithmic singularities while maintaining full accuracy under normal operating conditions.

Substituting (5) into (4a), the inverse kinematics model of the WMM considering task priority can be expressed as:

$$\boldsymbol{v} = \boldsymbol{J}^{\dagger}\dot{\boldsymbol{x}}_e + (\boldsymbol{J}_b\boldsymbol{\mathcal{N}})^{\dagger}\left(\dot{\boldsymbol{x}}_b - \boldsymbol{J}_b\boldsymbol{J}^{\dagger}\dot{\boldsymbol{x}}_e\right). \tag{6}$$

Note that $\boldsymbol{\mathcal{N}}(\boldsymbol{J}_b\boldsymbol{\mathcal{N}})^\dagger = (\boldsymbol{J}_b\boldsymbol{\mathcal{N}})^\dagger$, and therefore the redundant null-space projector is omitted for conciseness. When the reference trajectories of both the EE and the MB are specified, the dual-trajectory motion of the WMM can be achieved through (6).

3 Variable Admittance Control of WMMs

In this section, the proposed variable admittance controller considering both position and orientation compliance will be presented. Section 3.1 introduces the full pose compliance control scheme for a WMM system. Section 3.2 illustrates how to adjust the corresponding admittance parameters according to the detected interaction forces/torques.

3.1 Full Pose Compliance Rendered by an Admittance-based Control Scheme

To prevent damage to both the robot and the door during the door-opening process, the EE must achieve compliant contact with the door. Given the complexity of the actual environment, the design of the compliance control should simultaneously consider both positional compliance and orientational compliance at the EE. The kinematic model of the WMM, as expressed in (2) and (6), indicates that the design of the task-space velocity vector of the EE, denoted as $\dot{\boldsymbol{x}}_e$, is crucial for achieving EE-door compliance. The translational velocity of the EE can be obtained by solving the time derivative of its position, while the rotational angular velocity will be derived using a quaternion-based orientation planning method [31].

A standard quaternion can be defined as $\boldsymbol{\mathcal{Q}} = \{\eta, \boldsymbol{\epsilon}\} \in \mathbb{R}^4$, where η represents the scalar part of the quaternion, and $\boldsymbol{\epsilon} = [\epsilon_x, \epsilon_y, \epsilon_z]^{\mathrm{T}} \in \mathbb{R}^3$ denotes its vector part, indicating the direction of rotation. These four components satisfy the constraint $\eta^2+\epsilon_x^2+\epsilon_y^2+\epsilon_z^2 = 1$. Given the property of the rotation matrix $\boldsymbol{R}^{-1} = \boldsymbol{R}^{\mathrm{T}}$, the expression for the inverse quaternion $\boldsymbol{\mathcal{Q}}^{-1}$ is $\boldsymbol{\mathcal{Q}}^{-1} = \{\eta, -\boldsymbol{\epsilon}\}$. Therefore, if there exist two quaternions $\boldsymbol{\mathcal{Q}}_1 = \{\eta_1, \boldsymbol{\epsilon}_1\}$ and $\boldsymbol{\mathcal{Q}}_2 = \{\eta_2, \boldsymbol{\epsilon}_2\}$, whose corresponding rotation matrices are $\boldsymbol{R}_1$ and $\boldsymbol{R}_2$, respectively, the quaternion corresponding to the matrix product $\boldsymbol{R}_1\boldsymbol{R}_2$ can be calculated as:

$$\boldsymbol{\mathcal{Q}}_1 \otimes \boldsymbol{\mathcal{Q}}_2 = \left\{\eta_1\eta_2 - \boldsymbol{\epsilon}_1^{\mathrm{T}}\boldsymbol{\epsilon}_2,\ \eta_1\boldsymbol{\epsilon}_2 + \eta_2\boldsymbol{\epsilon}_1 + \boldsymbol{\epsilon}_1 \times \boldsymbol{\epsilon}_2\right\}, \tag{7}$$

where $\otimes$ denotes the quaternion multiplication operator, and $\times$ denotes the cross product. This operation ensures the correct composition of rotations in quaternion form.

To achieve quaternion-based orientation planning, it is first necessary to define an appropriate orientation error expression. If the rotation matrices $\boldsymbol{R}_d$ and $\boldsymbol{R}$ correspond to the quaternions $\boldsymbol{\mathcal{Q}}_d = \{\eta_d, \boldsymbol{\epsilon}_d\}$ and $\boldsymbol{\mathcal{Q}} = \{\eta, \boldsymbol{\epsilon}\}$, respectively, then according to (7), the orientation error defined by $\boldsymbol{R}_d\boldsymbol{R}^{\mathrm{T}}$ can be expressed in terms of quaternions as $\Delta\boldsymbol{\mathcal{Q}} = \{\Delta\eta, \Delta\boldsymbol{\epsilon}\}$, where $\Delta\boldsymbol{\mathcal{Q}} = \boldsymbol{\mathcal{Q}}_d \otimes \boldsymbol{\mathcal{Q}}^{-1}$. Based on this, the orientation error expression is defined as:

$$\boldsymbol{e}_O = \Delta\boldsymbol{\epsilon} = \eta\boldsymbol{\epsilon}_d - \eta_d\boldsymbol{\epsilon} - \boldsymbol{S}(\boldsymbol{\epsilon}_d)\boldsymbol{\epsilon}, \tag{8}$$

where $\boldsymbol{S}(\cdot)$ represents the skew-symmetric operator.

Combining with (1), it can be concluded that the WMM kinematic controller incorporating quaternion-based orientation planning is given by:

$$\boldsymbol{v} = \boldsymbol{J}^{\dagger} \begin{bmatrix} \dot{\boldsymbol{p}}_d + \boldsymbol{K}_P \boldsymbol{e}_P \\ \boldsymbol{\omega}_d + \boldsymbol{K}_O \boldsymbol{e}_O \end{bmatrix}, \tag{9}$$

where $\dot{\boldsymbol{p}}_d \in \mathbb{R}^3$ denotes the desired velocity vector, while $\boldsymbol{K}_P \in \mathbb{R}^{3\times3}$ represents a diagonal positive definite matrix corresponding to the position control gain. The position error vector, denoted as $\boldsymbol{e}_P \in \mathbb{R}^3$, is defined as $\boldsymbol{e}_P = \boldsymbol{p}_d - \boldsymbol{p}$, where $\boldsymbol{p}$ represents the actual EE position. Similarly, $\boldsymbol{\omega}_d \in \mathbb{R}^3$ denotes the desired angular velocity vector, and $\boldsymbol{K}_O \in \mathbb{R}^{3\times3}$ is a diagonal positive definite matrix representing the orientation control gain. The orientation error vector $\boldsymbol{e}_O \in \mathbb{R}^3$ is defined in (8). It should be noted that (9) mainly illustrates how to simultaneously control the EE's position and orientation. The last term on the right-hand side is essentially equivalent to $\dot{\boldsymbol{x}}_e$ in (6).

The actual EE velocity vector in (1) is given by $\dot{\boldsymbol{x}}_e = \left[\dot{\boldsymbol{p}}^{\mathrm{T}}, \boldsymbol{\omega}^{\mathrm{T}}\right]^{\mathrm{T}}$. If the precise parameters in the door-opening process are known, the desired trajectory of the EE can be directly planned, in which case (9) can serve as the EE's motion controller. However, to mitigate excessive contact forces caused by parameter identification errors, this study incorporates admittance control in the EE's trajectory planning.

The admittance control model for translational motion is relatively simple and can be expressed as:

$$\boldsymbol{f} = \boldsymbol{M}_P(\ddot{\boldsymbol{p}}_d - \ddot{\boldsymbol{p}}) + \boldsymbol{B}_P(\dot{\boldsymbol{p}}_d - \dot{\boldsymbol{p}}) + \boldsymbol{K}_P(\boldsymbol{p}_d - \boldsymbol{p}), \tag{10}$$

where $\boldsymbol{M}_P \in \mathbb{R}^{3\times3}$ represents the desired inertia of the translational admittance model, $\boldsymbol{B}_P \in \mathbb{R}^{3\times3}$ denotes the desired damping, and $\boldsymbol{K}_P \in \mathbb{R}^{3\times3}$ corresponds to the desired stiffness. Additionally, $\boldsymbol{f} \in \mathbb{R}^3$ represents the interaction force vector.

The essence of admittance control for rotational motion is to describe the compliance relationship between the EE torque $\boldsymbol{\tau} \in \mathbb{R}^3$ and the EE angular velocity $\boldsymbol{\omega} \in \mathbb{R}^3$. The primary challenge lies in the fact that the time integral of angular velocity, $\int \boldsymbol{\omega} \mathrm{d}t$, lacks physical significance and is unsuitable for representing rotational displacement and directional stiffness. Based on (8), the admittance model for rotational motion can be defined as [32]:

$$\begin{cases} \boldsymbol{\tau} = \boldsymbol{M}_O(\dot{\boldsymbol{\omega}}_d - \dot{\boldsymbol{\omega}}) + \boldsymbol{B}_O(\boldsymbol{\omega}_d - \boldsymbol{\omega}) + \boldsymbol{K}'_O \Delta\boldsymbol{\epsilon} \\ \boldsymbol{K}'_O = 2\boldsymbol{E}^{\mathrm{T}}(\Delta\eta, \Delta\boldsymbol{\epsilon})\boldsymbol{K}_O \\ \boldsymbol{E} = \Delta\eta\boldsymbol{I} - \boldsymbol{S}(\Delta\boldsymbol{\epsilon}) \end{cases}, \tag{11}$$

where $\boldsymbol{M}_O \in \mathbb{R}^{3\times3}$ represents the desired inertia of the rotational admittance model, $\boldsymbol{B}_O \in \mathbb{R}^{3\times3}$ denotes the desired damping, and $\boldsymbol{K}_O \in \mathbb{R}^{3\times3}$ corresponds to the desired stiffness. Additionally, $\boldsymbol{\tau} \in \mathbb{R}^3$ represents the EE's torque vector.

The time derivative of the quaternion representing the orientation can be transformed into the EE's angular velocity through:

$$\begin{cases} \dot{\eta} = -\frac{1}{2}\boldsymbol{\epsilon}^{\mathrm{T}}\boldsymbol{\omega} \\ \dot{\boldsymbol{\epsilon}} = \frac{1}{2}\left(\eta\boldsymbol{I} - \boldsymbol{S}(\boldsymbol{\epsilon})\right)\boldsymbol{\omega} \end{cases}. \tag{12}$$

Equations (10) and (11) convert the interaction forces/torques between the EE and the door into the corresponding desired displacement/rotation. By substituting this information into (9), the joint velocities that ensure the desired compliance at the EE can be obtained.

3.2 Design of Variable Admittance Parameters

To improve the generality of the WMM in door-opening tasks and enable smoother rotation of doors with varying resistance torques, this study introduces variable admittance control by allowing the fixed admittance in (10) and (11) to be continuously adjusted based on the interaction forces and torques. Notably, the position and orientation admittance are designed in a decoupled manner, enabling their independent application in compliance control. The following discussion focuses on the design of position admittance parameters as an example to illustrate the variable admittance control process, while the design of orientation admittance parameters follows a similar approach.

First, a regulating function α is introduced, which is expressed as:

$$\alpha = \frac{\boldsymbol{f}^{\mathrm{T}}\boldsymbol{f}}{\xi + |\boldsymbol{f}^{\mathrm{T}}\boldsymbol{f}|} \tag{13}$$

with $\boldsymbol{f}$ being a (3×1) interaction force vector, as expressed in (10) and ξ being a positive constant. The function α smoothly determines whether the EE has contacted the door handle. Its values are restricted to the interval $[0, 1)$, approaching zero when no forces are detected and asymptotically approaching one as forces appear. This regulating function enables rapid and continuous adaptation of the restoring force magnitude. Redefining the desired stiffness in (10) as an adaptive gain:

$$\boldsymbol{K}_P(\alpha) = (1 - \alpha)\boldsymbol{K}_{P0} \tag{14}$$

with $\boldsymbol{K}_{P0} \in \mathbb{R}^{3\times3}$ being a fixed stiffness matrix to follow the reference position. The key advantage of this approach is that it seamlessly integrates predefined door-opening motions with externally guided trajectories without requiring any modifications to the control scheme or matrix values.

To further enhance the robot's adaptability in different interaction scenarios, we employ a variable damping strategy that depends on both motion and contact conditions. Inspired by [33], which suggests decreasing damping for large/fast movements and increasing it for small/precise actions, we first compute a candidate damping

matrix as:

$$\bar{\boldsymbol{B}}_P(\alpha, \boldsymbol{f}, \dot{\boldsymbol{p}}) = \boldsymbol{B}_{P0} - \mathrm{diag}\{\alpha\beta_1|\dot{\boldsymbol{p}}| + \beta_2|\boldsymbol{f}|\}, \tag{15}$$

where α is defined in (13), and β_1, β_2 are positive weighting coefficients. Note that the subtraction in (15) implements the intended reduction of damping during fast motions and the increase of effective compliance under larger contact forces.

To guarantee physically meaningful damping and avoid negative diagonal entries, the candidate matrix $\bar{\boldsymbol{B}}_P$ is element-wise saturated from below. A straightforward and implementation-friendly form is given by:

$$\boldsymbol{B}_P(\alpha, \boldsymbol{f}, \dot{\boldsymbol{p}}) = \mathrm{diag}\{\max(b_{\min},\ \bar{b}_1),\ \max(b_{\min},\ \bar{b}_2),\ \max(b_{\min},\ \bar{b}_3)\}, \tag{16}$$

where $\bar{b}_i$ denotes the i-th diagonal element of $\bar{\boldsymbol{B}}_P$ in (15) and $b_{\min} > 0$ is a small design constant that sets the minimum allowable damping for each axis. This saturation prevents negative or excessively small damping values while preserving the adaptive trend indicated by (15). This formulation ensures positive damping in all conditions while maintaining smooth adaptive behavior across different interaction phases.

Meanwhile, to maintain the stability of the compliance control system, this study keeps the ratio between inertia and damping constant, which is expressed as:

$$\boldsymbol{M}_P = \frac{\boldsymbol{M}_{P0}\boldsymbol{B}_P}{\boldsymbol{B}_{P0}}, \tag{17}$$

where $\boldsymbol{M}_{P0}$ denotes a fixed inertia matrix, which maintains a specific ratio with the fixed $\boldsymbol{B}_{P0}$ to ensure both system stability and compliant door-opening performance.

To provide formal guarantees of the proposed variable admittance control scheme, a Lyapunov-based stability analysis is presented. For clarity, the derivation below considers the translational admittance dynamics; the orientation case follows an analogous process using quaternion errors $\Delta\boldsymbol{\epsilon}$.

Assumption 1: The interaction force $\boldsymbol{f}(t)$ is bounded with $\|\boldsymbol{f}(t)\| \leqslant \boldsymbol{F}_{\max}$.

Assumption 2: The variables $\boldsymbol{B}_P(t)$ and $\boldsymbol{K}_P(t)$ are symmetric and uniformly positive semi-definite, satisfying $\boldsymbol{B}_P(t) \succeq b_{\min}\boldsymbol{I}_3$ and $\boldsymbol{K}_P(t) \succeq 0$.

Assumption 3: The parameter derivatives are bounded: $\|\dot{\boldsymbol{M}}_P(t)\| \leqslant m_M$, $\|\dot{\boldsymbol{B}}_P(t)\| \leqslant m_B$, and $\|\dot{\boldsymbol{K}}_P(t)\| \leqslant m_K$, with $m_M, m_B, m_K > 0$.

Assumption 4: Parameter variations are sufficiently slow so that the induced energy change is dominated by the intrinsic dissipation of $\boldsymbol{B}_P$, *i.e.*,

$$\tfrac{1}{2}\dot{\tilde{\boldsymbol{p}}}^{\mathrm{T}}\dot{\boldsymbol{M}}_P\dot{\tilde{\boldsymbol{p}}} + \tfrac{1}{2}\tilde{\boldsymbol{p}}^{\mathrm{T}}\dot{\boldsymbol{K}}_P\tilde{\boldsymbol{p}} \leqslant \gamma\,\dot{\tilde{\boldsymbol{p}}}^{\mathrm{T}}\boldsymbol{B}_P\dot{\tilde{\boldsymbol{p}}} + C, \tag{18}$$

where $0 \leqslant \gamma < 1$ and $C \geqslant 0$ is a known bound.

According to the translational admittance model in (10), we define $\tilde{\boldsymbol{p}} = \boldsymbol{p}_d - \boldsymbol{p}$ and $\dot{\tilde{\boldsymbol{p}}} = \dot{\boldsymbol{p}}_d - \dot{\boldsymbol{p}}$ denote the tracking errors.

Define the candidate Lyapunov function as:

$$V(t) = \tfrac{1}{2}\dot{\tilde{\boldsymbol{p}}}^{\mathrm{T}}\boldsymbol{M}_P(t)\dot{\tilde{\boldsymbol{p}}} + \tfrac{1}{2}\tilde{\boldsymbol{p}}^{\mathrm{T}}\boldsymbol{K}_P(t)\tilde{\boldsymbol{p}}, \tag{19}$$

then, differentiating $V(t)$ and substituting the closed-loop admittance dynamics (10) yields:

$$\dot{V} = -\dot{\tilde{\boldsymbol{p}}}^{\mathrm{T}} \boldsymbol{B}_P \dot{\tilde{\boldsymbol{p}}} + \tfrac{1}{2}\dot{\tilde{\boldsymbol{p}}}^{\mathrm{T}} \dot{\boldsymbol{M}}_P \dot{\tilde{\boldsymbol{p}}} + \tfrac{1}{2}\tilde{\boldsymbol{p}}^{\mathrm{T}} \dot{\boldsymbol{K}}_P \tilde{\boldsymbol{p}} + \Phi(t), \tag{20}$$

where $\Phi(t)$ collects bounded modeling terms.

Using *Assumption 4*, we obtain

$$\dot{V} \leqslant -(1-\gamma)\, \dot{\tilde{\boldsymbol{p}}}^{\mathrm{T}} \boldsymbol{B}_P \dot{\tilde{\boldsymbol{p}}} + (C + \Phi(t))\,. \tag{21}$$

Because $\boldsymbol{B}_P \succeq b_{\min}\boldsymbol{I}$ and $\Phi(t)$ is bounded, $V(t)$ is non-increasing except for a bounded residual. Therefore, $\tilde{\boldsymbol{p}}$ and $\dot{\tilde{\boldsymbol{p}}}$ remain bounded, and with vanishing disturbances $\dot{\tilde{\boldsymbol{p}}} \to 0$ as $t \to \infty$, ensuring closed-loop stability.

It is worth mentioning that *Assumption 4* can be practically verified by limiting the adaptation rate of $\alpha(t)$ so that

$$\|\dot{\boldsymbol{M}}_P\| \leqslant 2\gamma\, b_{\min}, \qquad \|\dot{\boldsymbol{K}}_P\| \leqslant 2\gamma\, \lambda_{\min}(\boldsymbol{K}_P). \tag{22}$$

This can be achieved by clamping $\boldsymbol{B}_P, \boldsymbol{K}_P$ within predefined ranges and filtering $\alpha(t)$ to ensure smooth parameter evolution.

4 Experimental Setup and Results

To verify the efficiency of the proposed approach, several experiments have been conducted. The experimental setup is introduced in Section 4.1. Section 4.2 presents the preliminary results of the task-priority-based redundancy resolution approach of a redundant WMM. Section 4.3 verifies the proposed variable admittance controller's performance by achieving a door-opening task in a constrained environment with an obstacle on the ground.

4.1 Experimental Setup

In this study, an omnidirectional WMM with a holonomic constraint on the base is utilized, as depicted in Fig. 1, where $\{\Sigma_w\}$ represents the world frame, $\{\Sigma_b\}$ denotes the frame of the MB, and $\{\Sigma_e\}$ corresponds to the frame of the EE. The system comprises a custom-built four-wheel MB and a 7-DOF ultra-lightweight robotic manipulator, Kinova Gen3 (Kinova Robotics, Canada). The MB is equipped with two pairs of Mecanum wheels, enabling omnidirectional motion. This configuration enhances operational efficiency by reducing overall execution time and minimizing idle periods when adjusting the robot's pose for a given task [34]. The interaction forces and torques between the EE and the door are estimated based on feedback from the manipulator's joint torque sensors, as detailed in our previous work [17]. The motion planning and control code was developed in C++, adopting the Eigen library for algebraic computations. The experiments were performed in the ROS environment on a Intel(R) Xeon(R) CPU X5550 @ 2.67 GHz, with 16 GB of RAM.

In subsequent experiments, the Cartesian space dimensions for the EE and MB are defined as 6 and 3, respectively, accounting for both position and orientation. Consequently, the dimensions of $\boldsymbol{x}_e$ and $\boldsymbol{x}_b$ in (6) are 6 and 2, respectively. The initial generalized coordinate vector of the WMM is given by $\boldsymbol{q}_0 = [0, 0, 0, 0, 0, 0, 53\pi/180, 0, 37\pi/180, 0]^{\mathrm{T}}$ rad, where the first three parameters correspond to the MB. The initial poses of the EE and MB in the world frame are obtained using the WMM forward kinematics, yielding $\boldsymbol{x}_{e0} = [0.538\,\mathrm{m}, -0.0246\,\mathrm{m}, 0.895\,\mathrm{m}, -\pi/2\,\mathrm{rad}, \pi/2\,\mathrm{rad}, -\pi/2\,\mathrm{rad}]^{\mathrm{T}}$ and $\boldsymbol{x}_{b0} = [0, 0, 0]^{\mathrm{T}}$, respectively. It should be noted that the orientation of the EE is presented based on XYZ Euler angles [35] and then converted into a quaternion, facilitating a clearer representation of the desired EE orientation.

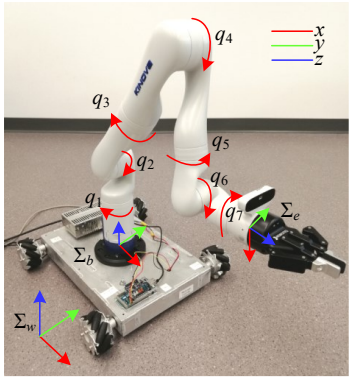

Fig. 1: Experimental setup.

4.2 Experiments for Task-priority-based Redundancy Resolution of WMM

In this experiment, the desired trajectory vectors of the EE and MB are defined as $\boldsymbol{x}_e^d(t) = \boldsymbol{x}_{e0} + [R_e \sin(\pi/10t), -R_e/2 \sin(\pi/5t), 0, 0, 0, 0]^{\mathrm{T}}$ and $\boldsymbol{x}_b^d(t) = \boldsymbol{x}_{b0} + [R_b \cos(\pi/10t) - R_b, R_b \sin(\pi/10t), 0]^{\mathrm{T}}$, respectively. Since the WMM in this study employs a velocity-level planning and control approach, a PD control method similar to that in (9) is used to ensure accurate dual trajectory tracking of the EE and MB poses. The control gains are set to $\boldsymbol{K}_e = 40\boldsymbol{I}_{6\times6}$ and $\boldsymbol{K}_b = 20\boldsymbol{I}_{3\times3}$, respectively. Here, two scenarios with different trajectories for the EE and MB are considered. In the first scenario, both trajectories can be successfully tracked. In the second scenario, simultaneous tracking of both trajectories is not feasible. Given the higher task priority of the EE over the MB, tracking of the EE trajectory is prioritized. The trajectory parameters for the two scenarios are as follows. **Scenario 1:** $R_e = 0.05\,\mathrm{m}$, $R_b = 0.05\,\mathrm{m}$; **Scenario 2:** $R_e = 0.1\,\mathrm{m}$, $R_b = 0.1\,\mathrm{m}$. It is important to note that the experimental data were collected over two cycles to ensure a reliable assessment of tracking performance and consistency.

Table 1: Maximum and RMS values of trajectory tracking errors in the two scenarios.

	$x_e(x)/10^{-3}$m		$x_e(y)/10^{-3}$m		$x_b(x)/10^{-3}$m		$x_b(y)/10^{-3}$m	
	Max.	RMS	Max.	RMS	Max.	RMS	Max.	RMS
Scenario 1	0.283	0.0828	0.416	0.176	0.624	0.323	0.643	0.305
Scenario 2	0.676	0.0891	0.464	0.177	83.17	39.43	14.66	5.65

Snapshots of the WMM in **Scenario 1** are shown in Fig. 2, clearly illustrating its poses at different time instances under this condition. To avoid redundancy, experimental snapshots for **Scenario 2** are not displayed, as its results exhibit similar patterns to those in **Scenario 1**. The experimental results for the two scenarios are shown in Figs. 3-5. Notably, since the desired position trajectory of the EE is defined in the $x-y$ plane, the tracking results for the z-direction and all orientation components are omitted.

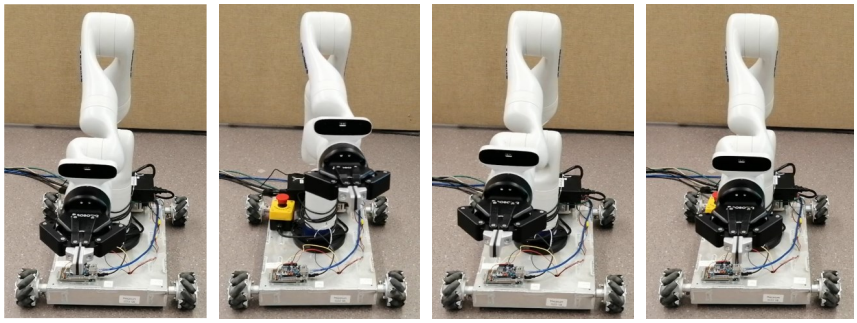

(a) 0 s (b) 5 s (c) 15 s (d) 20 s

Fig. 2: Sequence diagram of the WMM in **Scenario 1**.

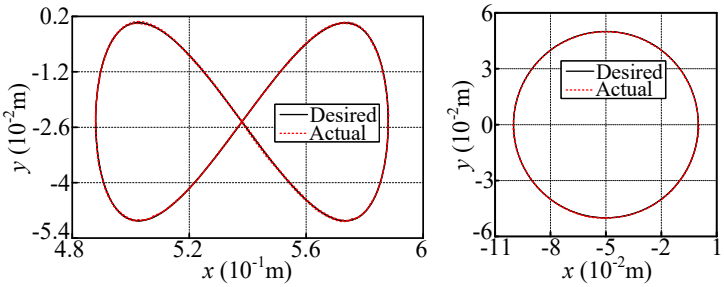

(a) Trajectory of EE (b) Trajectory of MB

Fig. 3: Trajectory tracking of EE and MB in **Scenario 1**.

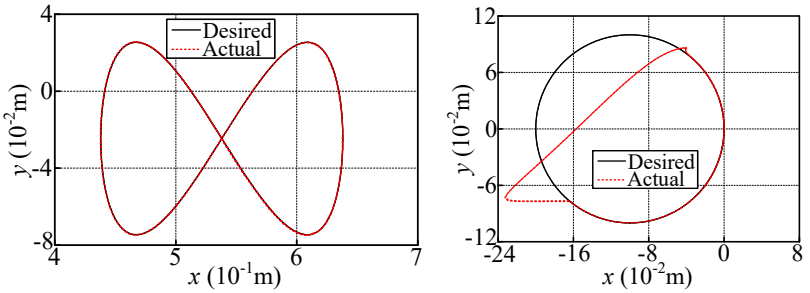

(a) Trajectory of EE (b) Trajectory of MB

Fig. 4: Trajectory tracking of EE and MB in **Scenario 2**.

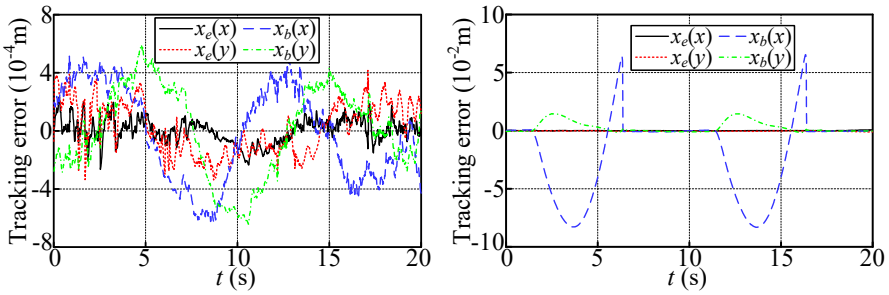

(a) **Scenario 1** (b) **Scenario 2**

Fig. 5: Trajectory tracking errors in the two scenarios.

Figs. 3 and 5b, along with Table 1, demonstrate that when the WMM had sufficient redundancy to simultaneously execute the control required for both the EE and MB, their respective trajectories were successfully tracked. The maximum tracking errors for the EE and MB were 0.416×10^{-3} m and 0.643×10^{-3} m, corresponding to 0.83% and 0.64% of their motion ranges, respectively. Additionally, the tracking errors in each direction were recorded, and their RMS values were computed to provide a more comprehensive evaluation of tracking performance. These results further validate the effectiveness of the proposed method in tracking dual trajectories.

In **Scenario 2**, as the desired trajectories of the EE and MB increased, the WMM lacked sufficient redundancy to track both simultaneously. Given the higher tracking priority of the EE trajectory, the MB was unable to follow its desired path (as shown in Fig. 4). According to Fig. 5, the MB was forced to deviate by approximately 8×10^{-2} m in the x-direction, while the maximum tracking error of the EE remained within 7×10^{-3} m. These results demonstrate that the proposed dual-trajectory tracking method remains effective even when simultaneous tracking of both trajectories is not feasible.

4.3 Experiments for Compliant Door-opening Task

Compliance control is a key aspect of the door-opening task, effectively preventing excessive contact forces. Section 4.2 demonstrated the feasibility of the proposed dual-trajectory tracking method, where the MB trajectory helps avoid ground obstacles, while the EE trajectory enables the rotation of the door handle. This section focuses on implementing compliant handle rotation using the variable admittance control method introduced in Section 3.

To achieve smooth and compliant rotation of the door handle, the variable admittance parameters were determined through repeated trials and are listed in Table 2. For variable stiffness and damping, the weights were set as $\xi = 80$, $\beta_1 = 100$, $\beta_2 = 50$ and $b_{\min} = 100$ for position; and $\xi = 1$, $\beta_1 = 50$, $\beta_2 = 30$ and $b_{\min} = 1$ for orientation.

Table 2: Admittance parameters in the experiment.

Parameter	Value
$\boldsymbol{K}_{P0}$	$\mathrm{diag}(1600, 1600, 1200)$ N/m
$\boldsymbol{B}_{P0}$	$\mathrm{diag}(800, 800, 600)$ Ns/m
$\boldsymbol{M}_{P0}$	$\mathrm{diag}(400, 400, 300)$ Ns^2/m
$\boldsymbol{K}_{O0}$	$\mathrm{diag}(10, 10, 10)$ Nm/rad
$\boldsymbol{B}_{O0}$	$\mathrm{diag}(5, 5, 5)$ Nms/rad
$\boldsymbol{M}_{O0}$	$\mathrm{diag}(3, 3, 3)$ Nms^2/rad

To validate the effectiveness of the proposed EE force/torque estimation method, experiments were conducted using a wrist-mounted F/T sensor (Axia80-ZC22, ATI Industrial Automation, Apex, NC, USA) as the ground truth reference. The experimental setup is shown in Fig. 6. During the experiment, the operator applied external forces and torques to the EE while the admittance controller was activated with the parameters listed in Table 2. Both the desired force/torque and desired trajectory were set to zero, allowing the EE to remain compliant and freely follow the operator's motion.

Representative results are shown in Figs. 7 and 8, while the quantitative estimation errors are summarized in Table 3. The maximum absolute force estimation errors in the x-, y-, and z-directions were 5.33 N, 5.16 N, and 2.41 N, respectively, corresponding to RMS errors of 4.78%, 6.77%, and 6.28% of the maximum measured force magnitudes. For torques, the maximum estimation error occurred in the z-axis (0.11 Nm), and the maximum RMS error appeared in the y-axis (0.029 Nm). These results quantitatively demonstrate that the proposed estimation approach can accurately capture the contact interaction with limited bias and noise across all directions.

The experimental results indicate that the proposed joint-torque-based force estimation introduces only minor bias and moderate noise, primarily arising from model uncertainties and sensor quantization. These estimation errors and the small communication delay observed in the loop have a negligible effect on system performance. Owing to the variable admittance design, the controller preserves passivity and stability in the presence of such imperfections. The damping component effectively attenuates

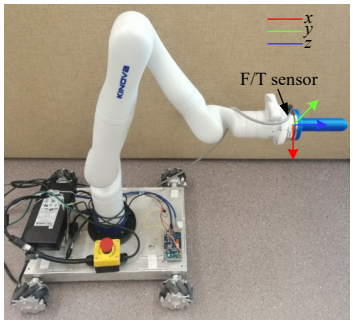

Fig. 6: Experimental setup for interaction force estimation.

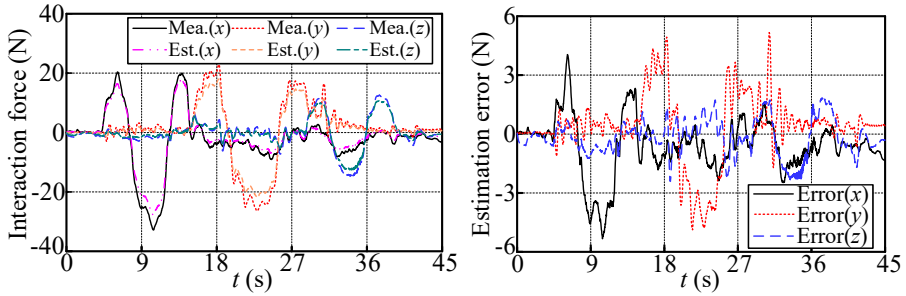

(a) Interaction force (b) Estimation error

Fig. 7: Comparison of estimated force and measured force.

Table 3: Maximum and RMS errors of force/torque estimation.

Component	Maximum error	RMS error
Translational x	5.33 N	1.57 N
Translational y	5.16 N	1.79 N
Translational z	2.41 N	0.92 N
Rotational x	0.088 Nm	0.025 Nm
Rotational y	0.089 Nm	0.029 Nm
Rotational z	0.11 Nm	0.028 Nm

high-frequency noise, while the adaptive stiffness adjustment prevents excessive reaction forces caused by transient estimation bias. No instability was observed during the experiments, confirming that the proposed control framework remains robust against moderate estimation errors and latency.

To validate the effectiveness and advantages of the proposed variable admittance control method, the first step is to demonstrate its capability in interaction operations, even when the robot follows a predefined task (e.g., hand-guiding). To analyze the results, simple unidirectional experiments were conducted. Figs. 9 and 10 depict a

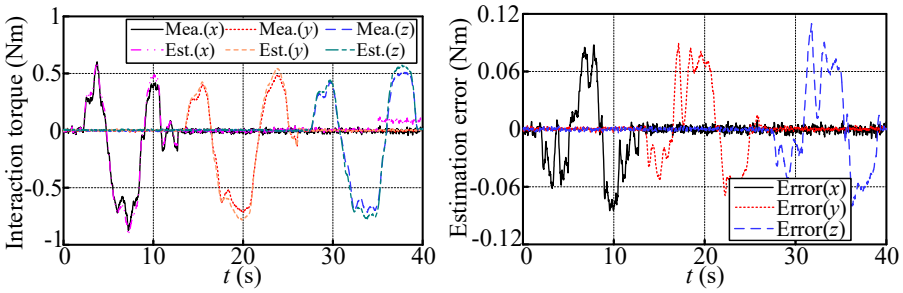

(a) Interaction torque (b) Estimation error

Fig. 8: Comparison of estimated torque and measured torque.

scenario in which an operator moves the EE approximately 0.02 m in the x-direction, while the robot maintains its predefined task of preserving the initial pose. The admittance parameters for this experiment are set according to the x-direction values in Table 2.

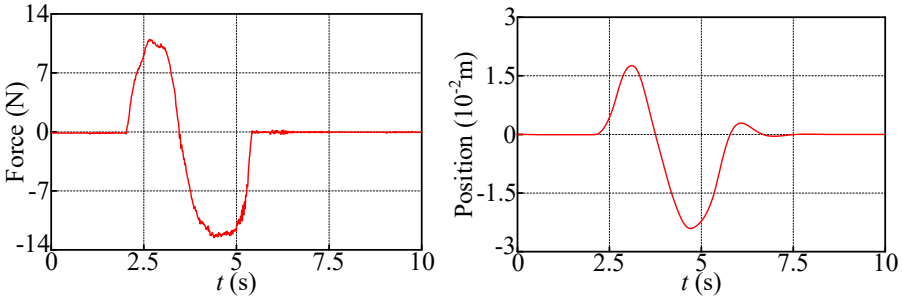

(a) x-direction force (b) x-direction position

Fig. 9: Force and position in the one-dimensional operator movement.

From Figs. 9 and 10, it can be observed that once a contact force was detected, the parameter α gradually increased. This adjustment reduced the predefined stiffness and damping, preventing the robot from interfering with the operator's movement. Conversely, when no contact force was present, such as during the intervals 0-1.95 s and 5.42-10 s, α gradually returned to zero. This restoration ensured high stiffness in the robot, allowing it to accurately track the desired EE trajectory.

To further analyze the interaction and demonstrate the effectiveness of incorporating the parameter α within the variable admittance scheme, comparative experiments were conducted using both a fixed admittance parameter setting and an energy tank-based variable admittance control scheme. The fixed parameters were kept identical to those in the variable admittance case when no contact force was present, ensuring the validity of the comparison. The energy tank-based variable admittance scheme

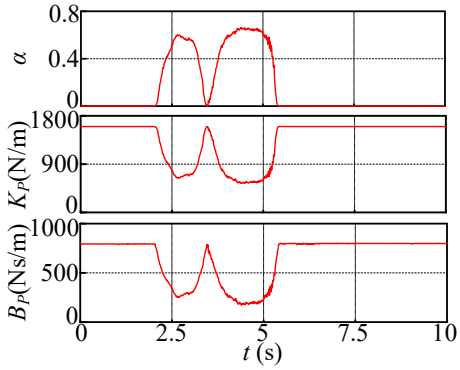

Fig. 10: Parameter variation in the one-dimensional operator movement.

was implemented following the passivity modulation principle described in [36, 37]. The base admittance parameters were kept identical to those in the fixed-admittance case, while parameter adaptation was governed by the stored tank energy to ensure passive and stable interaction. The detailed control design and stability analysis can be found in the cited references. The experimental results are shown in Fig. 11.

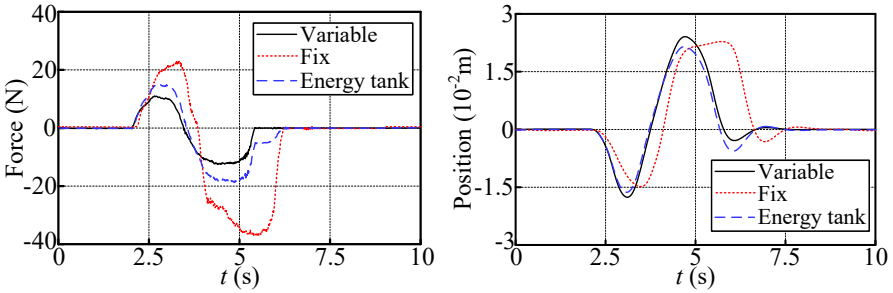

(a) x-direction forces (b) x-direction positions

Fig. 11: Comparison of fixed, variable, and energy tank-based admittance control in one-dimensional motion.

Fig. 11b presents the displacement in the x-direction for all three experiments, showing that the EE exhibited nearly identical displacements of approximately 2×10^{-2} m across the three cases. Moreover, in each scenario, the system responded to the reference position with the characteristics of a second-order system.

Fig. 11a illustrates the interaction forces required to achieve the EE motion depicted in Fig. 11b. Under the fixed admittance condition, the maximum interaction force occurred at approximately 5.39 s, reaching 37.14 N. Under the energy tank–based variable admittance condition, the peak force appeared at around 4.83 s with a magnitude of 16.37 N. In contrast, under the proposed variable admittance condition, the peak interaction force was further reduced to 12.63 N at approximately 4.39 s—only

34% of that in the fixed admittance case and 77% of that in the energy tank–based case. This demonstrates that the proposed controller more effectively regulates contact dynamics and achieves smoother, more compliant interaction.

Additionally, the work exerted by the operator along the x-axis was computed as the integral of the applied power, $\int_0^t p_x \, \mathrm{d}\tau$, yielding 0.94 J for the fixed-admittance condition, 0.43 J for the energy tank–based condition, and 0.36 J for the proposed variable-admittance condition. This progressive reduction further confirms the superior efficiency of the proposed control method in minimizing operator effort and energy consumption during human–robot interaction.

To further validate the consistency and reliability of the results, ten repeated trials were conducted for each control strategy under identical experimental conditions. The quantitative metrics considered include the peak interaction force, RMS interaction force, and the EE compliance response (*i.e.*, the displacement induced by external forces), as well as the estimated energy consumption. The mean values and standard deviations across trials are summarized in Table 4.

Table 4: Quantitative comparison of admittance control methods over 10 trials.

Metric	Fixed admittance	Energy tank–based	Proposed variable
Peak force/N	35.34 ± 4.82	15.36 ± 2.41	$\mathbf{11.87 \pm 1.81}$
RMS force/N	14.82 ± 2.21	6.75 ± 0.89	$\mathbf{5.43 \pm 0.52}$
EE compliance/mm	20.43 ± 3.21	21.24 ± 2.77	$\mathbf{21.70 \pm 2.48}$
Energy consumption/J	0.92 ± 0.11	0.44 ± 0.07	$\mathbf{0.36 \pm 0.05}$

The results indicate that the proposed variable admittance control achieves the lowest mean peak and RMS interaction forces, while producing a compliant EE response similar to or slightly larger than the energy tank-based method, reflecting the system's smooth adaptation to operator input. These results confirm the robustness and statistical significance of the observed improvement in interaction performance.

Then, the proposed method was applied to a door-opening experiment, with experimental parameters set as described in this section. In this experiment, we assumed that the basic environmental information, including obstacles, had already been acquired, and an initial Cartesian space trajectory had been planned. For details on the generation of the robot's door-opening trajectory, refer to our previous work [7]. A video demonstrating the experiment is attached to the manuscript for better visualization of the proposed method in action.

In MB control, its orientation was always maintained constant. Initially, the MB's position in the y-direction was adjusted to avoid obstacles. Subsequently, its position was planned to follow the EE's motion. Snapshots of the door-opening experiment are shown in Fig. 12, where (a) shows the initial pose of the WMM, (b) depicts the WMM avoiding obstacles and approaching the door handle, (c) illustrates the EE pressing the door handle, (d) presents the WMM pushing the door open, and (e) displays the final pose of the WMM.

The experimental results for both MB and EE are presented in Figs. 13 and 14. As shown in Fig. 13a, the entire door-opening process can be divided into five main

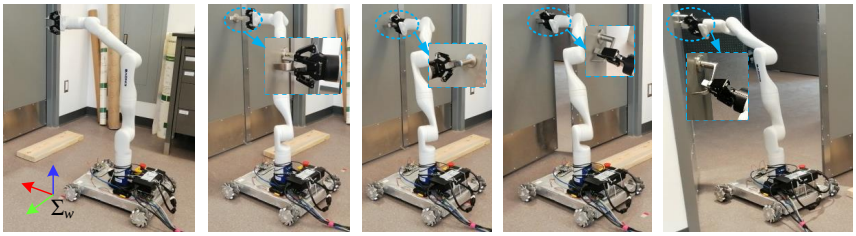

Fig. 12: Pictures of door-opening task based on dual trajectory tracking.

phases: (A) MB moves laterally to avoid obstacles, (B) WMM advances toward the door handle, (C) the gripper closes to grasp the handle, (D) EE presses the handle, and (E) the door is pushed open.

From Fig. 13, the maximum displacement of MB was approximately 1.15 m along the x-axis and 0.28 m along the y-axis. Additionally, as illustrated in Fig. 13b, the trajectory of MB effectively circumvented obstacles, demonstrating the feasibility of the proposed obstacle avoidance strategy.

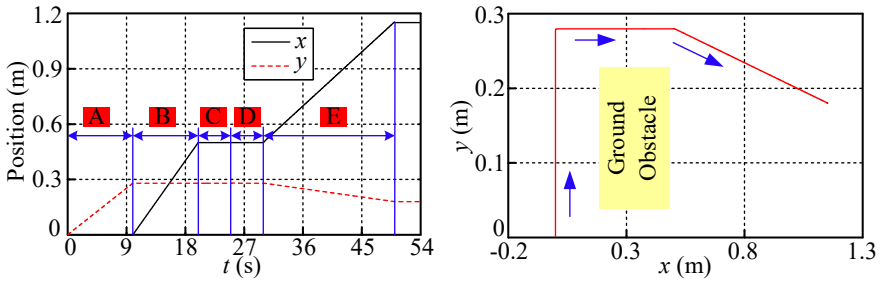

(a) Trajectory curve (b) Obstacle avoidance path

Fig. 13: Motion of MB during door-opening process.

As shown in Fig. 14a, while following the predefined EE trajectory, the EE could adjust its pose in real-time based on the applied force to mitigate additional interaction forces caused by trajectory deviations. This compliance, achieved through the proposed variable admittance control strategy, ensured that the maximum contact force between the EE and the door did not exceed 30 N. Furthermore, Fig. 14b indicates that the interaction torque between the EE and the door remained low throughout the experiment, staying below 0.6 Nm, while the EE's orientation closely matched its planned trajectory.

While the proposed variable admittance control framework supports both positional and orientational compliance (as introduced in Section 3), the door-opening task primarily relies on translational motion to rotate the handle. As shown in Fig. 14b, the EE's orientation closely follows the planned trajectory, and the interaction torques remain below 0.6 Nm throughout the task. This suggests that positional variable

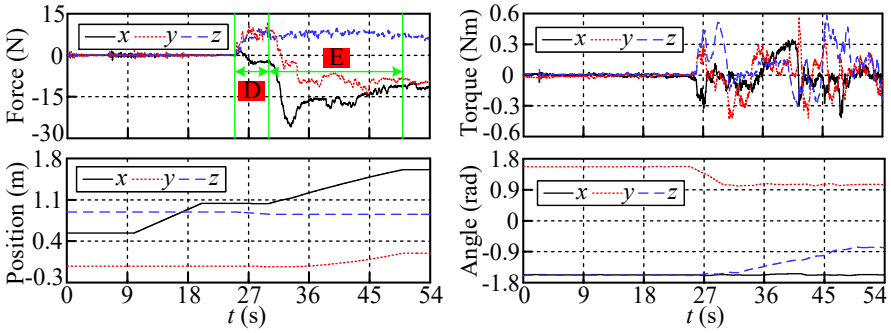

(a) Force and position (b) Torque and orientation

Fig. 14: Motion of EE during door-opening process.

admittance plays a dominant role in achieving compliant and safe door opening, whereas orientational compliance has a relatively minor effect in this scenario. Nevertheless, orientational admittance was implemented and tested, confirming that the EE orientation can be effectively regulated when needed.

It is worth noting that slight oscillations can be observed in the interaction force and torque profiles during Phases D–E in Fig. 14. These oscillations primarily arise from small delays and quantization noise in the joint-torque-based force estimation, as well as from abrupt variations in the admittance parameters when the contact condition changes. Additionally, the door–handle friction and structural stiffness introduce nonlinearities that amplify high-frequency responses within the admittance loop. Nevertheless, the amplitudes of these oscillations remain limited (below 5 N and 0.2 Nm), and the overall system remains stable without divergence.

To further mitigate this behavior, future work will focus on introducing a low-pass filter for the estimated forces and employing a smoother adaptation law for the variable stiffness and damping parameters to avoid abrupt parameter transitions. Increasing the controller update rate and incorporating model-based friction compensation will also be considered to suppress these residual oscillations and enhance control smoothness.

Overall, these results confirm the stable and compliant performance of the proposed control framework in the door-opening task. To further demonstrate the generality and robustness of the approach, we extended the experiments to three representative scenarios with different obstacle arrangements. For each scenario, four repeated trials were conducted under identical conditions to evaluate the repeatability and reliability of the results.

The experimental results are shown in Fig. 15, where only one representative trial is displayed for each scenario. As illustrated in Fig. 15b, Scenarios 1–3 were configured by shifting the obstacle along the y-axis by 0.4 m in the positive direction. Consequently, the MB trajectory was adjusted accordingly, as shown in Fig. 15a. It is noteworthy that in all scenarios, the manipulator successfully completed the door-opening task.

A statistical summary of all 12 trials (three scenarios $\times$ four repetitions) is presented in Table 5. The recorded quantitative metrics include the peak and RMS

tracking errors of the MB, as well as the peak EE forces and torques. These results validate the effectiveness of the proposed dual-trajectory tracking approach with integrated variable admittance control and further confirm its consistency and robustness under varying environmental configurations.

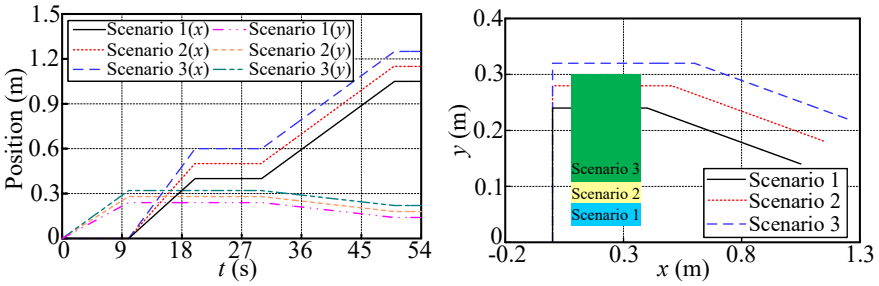

(a) Trajectory curve (b) Obstacle avoidance path

Fig. 15: Motion of MB during door-opening process for three scenarios.

Table 5: Quantitative results over three scenarios (four trials per scenario).

Metric	Scenario 1	Scenario 2	Scenario 3
Peak MB error/mm	0.62 ± 0.11	0.64 ± 0.12	0.62 ± 0.15
RMS MB error/mm	0.37 ± 0.07	0.35 ± 0.08	0.41 ± 0.06
Peak EE force/N	25.2 ± 3.4	23.5 ± 4.7	24.5 ± 3.9
Peak EE torque/Nm	0.56 ± 0.03	0.55 ± 0.03	0.55 ± 0.04

5 Conclusions

This paper presented a variable admittance control strategy integrated with dual-trajectory tracking, enabling a wheeled mobile manipulator (WMM) to perform compliant door-opening tasks in constrained environments. The proposed approach allowed the WMM to simultaneously track both the mobile base (MB) and end-effector (EE) trajectories while prioritizing high-level tasks through a task-priority framework. By adapting admittance parameters in real-time based on motion state and contact forces, the method effectively mitigated excessive interaction forces, enhancing compliance and robustness.

Experimental validation demonstrated the effectiveness of the proposed framework. In dual-trajectory tracking, the WMM maintained maximum errors below 0.7 mm for the EE and below 0.64 mm for the MB when redundancy allowed simultaneous execution. Unidirectional tests showed that the proposed variable admittance method reduced peak contact force to 12.63 N, compared to 37.14 N in the fixed-admittance case and 16.37 N for the energy tank–based method, with operator work decreasing

from 0.94 J to 0.36 J. In door-opening tasks, the EE interacted with forces below 30 N and torques under 0.6 Nm, successfully rotating the handle while the MB avoided obstacles. These results confirm that the framework enables compliant EE–MB coordination, mitigates excessive interaction forces, and ensures robust operation under varying conditions.

Future work will explore integrating bilateral teleoperation to leverage human decision-making for enhanced trajectory planning and adaptive interaction control.

Author Contributions. All authors were involved in the conception and design of the study. HX handled material preparation, investigation, control design, analysis, and validation. HX and YL wrote the original draft of the manuscript, and all authors provided feedback and revisions. All authors reviewed and approved the final manuscript.

Funding. This work was supported by the National Natural Science Foundation of China (52405025,52175007), the Natural Science Foundation of Jiangsu Province (BK20230889), the Shandong Provincial Natural Science Foundation (ZR2024YQ035), Canada Foundation for Innovation (CFI), and the Natural Sciences and Engineering Research Council (NSERC) of Canada.

Data Availability. The datasets generated and analyzed during the current study are available from the corresponding author on reasonable request.

Declarations

Conflicts of Interest/Competing Interests. The authors declare that they have no conflict of interest.

Ethics Approval. Not applicable.

Consent to Participate. Not applicable.

Consent for Publication. The authors declare that they consent to publish this article.

References

[1] Xing, H., Torabi, A., Ding, L., Gao, H., Deng, Z., Tavakoli, M.: Enhancement of force exertion capability of a mobile manipulator by kinematic reconfiguration. IEEE Robotics and Automation Letters **5**(4), 5842–5849 (2020)

[2] Arduengo, M., Torras, C., Sentis, L.: Robust and adaptive door operation with a mobile robot. Intelligent Service Robotics **14**(3), 409–425 (2021)

[3] Kang, G., Seong, H., Lee, D., Shim, D.H.: A versatile door opening system with mobile manipulator through adaptive position-force control and reinforcement learning. Robotics and Autonomous Systems **180**, 104760 (2024)

[4] Wang, G., Wang, W., Ding, P., Liu, Y., Wang, H., Fan, Z., Bai, H., Hongbiao, Z., Du, Z.: Development of a search and rescue robot system for the underground building environment. Journal of Field Robotics **40**(3), 655–683 (2023)

[5] Tavakoli, M., Carriere, J., Torabi, A.: Robotics, smart wearable technologies, and autonomous intelligent systems for healthcare during the covid-19 pandemic: An analysis of the state of the art and future vision. Advanced intelligent systems **2**(7), 2000071 (2020)

[6] Ahmad, S., Zhang, H., Liu, G.: Multiple working mode control of door-opening with a mobile modular and reconfigurable robot. IEEE/ASME Transactions On Mechatronics **18**(3), 833–844 (2012)

[7] Xing, H., Xia, K., Ding, L., Gao, H., Liu, G., Deng, Z.: Unknown geometrical constraints estimation and trajectory planning for robotic door-opening task with visual teleoperation assists. Assembly Automation **39**(3), 479–488 (2019)

[8] Karayiannidis, Y., Smith, C., Barrientos, F.E.V., Ögren, P., Kragic, D.: An adaptive control approach for opening doors and drawers under uncertainties. IEEE Transactions on Robotics **32**(1), 161–175 (2016)

[9] Wu, W., Liu, W.: Adaptive door opening control algorithm of bio-inspired mobile manipulator based on synchronous sensing. Frontiers in Bioengineering and Biotechnology **9**, 821981 (2022)

[10] Garcia-Hernando, G., Johns, E., Kim, T.-K.: Physics-based dexterous manipulations with estimated hand poses and residual reinforcement learning. In: 2020 IEEE/RSJ International Conference on Intelligent Robots and Systems (IROS), pp. 9561–9568 (2020). IEEE

[11] Raibert, M.H., Craig, J.J.: Hybrid Position/Force Control of Manipulators. Journal of Dynamic Systems, Measurement, and Control **103**(2), 126–133 (1981)

[12] Hogan, N.: Impedance control: An approach to manipulation: Parts I-III. Journal of Dynamic System, Measurement, and Control **107**(1), 1–24 (1985)

[13] Chen, L., Lai, P., Wang, Y., Dong, Y.: Fuzzy adaptive variable impedance control on deformable shield of defecation smart care robot. Biomimetic Intelligence and Robotics **5**(2), 100214 (2025)

[14] Ott, C., Mukherjee, R., Nakamura, Y.: Unified impedance and admittance control. In: IEEE International Conference on Robotics and Automation, pp. 554–561 (2010)

[15] Wu, Q., Chen, Y.: Variable admittance time-delay control of an upper limb rehabilitation robot based on human stiffness estimation. Mechatronics **90**, 102935 (2023)

[16] Rhee, I., Kang, G., Moon, S.J., Choi, Y.S., Choi, H.R.: Hybrid impedance and admittance control of robot manipulator with unknown environment. Intelligent Service Robotics **16**(1), 49–60 (2023)

[17] Xing, H., Torabi, A., Ding, L., Gao, H., Deng, Z., Mushahwar, V.K., Tavakoli, M.: An admittance-controlled wheeled mobile manipulator for mobility assistance: Human–robot interaction estimation and redundancy resolution for enhanced force exertion ability. Mechatronics **74**, 102497 (2021)

[18] Tu, Y., Zhu, A., Song, J., Shen, H., Shen, Z., Zhang, X., Cao, G.: An adaptive sliding mode variable admittance control method for lower limb rehabilitation exoskeleton robot. Applied Sciences **10**(7), 2536 (2020)

[19] Ding, L., Xing, H., Torabi, A., Mehr, J.K., Sharifi, M., Gao, H., Mushahwar, V.K., Tavakoli, M.: Intelligent assistance for older adults via an admittance-controlled wheeled mobile manipulator with task-dependent end-effectors. Mechatronics **85**, 102821 (2022)

[20] Sharkawy, A.-N., Koustoumpardis, P.N.: Human–robot interaction: A review and analysis on variable admittance control, safety, and perspectives. Machines **10**(7), 591 (2022)

[21] Lee, D., Ko, D., Kim, M.J., Chung, W.K.: Bidirectional energy flow modulation for passive admittance control. IEEE Transactions on Robotics **40**, 3917–3932 (2024)

[22] Han, L., Zhao, L., Huang, Y., Xu, W.: Variable admittance control for safe physical human–robot interaction considering intuitive human intention. Mechatronics **97**, 103098 (2024)

[23] Dietrich, A., Ott, C., Albu-Schäffer, A.: An overview of null space projections for redundant, torque-controlled robots. The International Journal of Robotics Research **34**(11), 1385–1400 (2015)

[24] Hassan, A.A., El-Habrouk, M., Deghedie, S.: Inverse kinematics of redundant manipulators formulated as quadratic programming optimization problem solved using recurrent neural networks: A review. Robotica **38**(8), 1495–1512 (2020)

[25] Sandakalum, T., Ang Jr, M.H.: Motion planning for mobile manipulators—a systematic review. Machines **10**(2), 97 (2022)

[26] Wang, G., Ma, H., Wang, H., Ding, P., Bai, H., Xu, W., Wang, W., Du, Z.: Reactive mobile manipulation based on dynamic dual-trajectory tracking. Robotics and Autonomous Systems **172**, 104589 (2024)

[27] Xing, H., Ding, L., Gao, H., Li, W., Tavakoli, M.: Dual-user haptic teleoperation of complementary motions of a redundant wheeled mobile manipulator considering

task priority. IEEE Transactions on Systems, Man, and Cybernetics: Systems **52**(10), 6283–6295 (2022)

[28] Mashali, M., Alqasemi, R., Dubey, R.: Task priority based dual-trajectory control for redundant mobile manipulators. In: IEEE International Conference on Robotics and Biomimetics, pp. 1457–1462 (2014)

[29] Fukumoto, Y., Jinnai, M., Bando, S., Takenaka, M., Kobayashi, H.: Door opening and closing considering forces using a mobile manipulator with an admittance controlled arm. Journal of Robotics and Mechatronics **35**(6), 1573–1582 (2023)

[30] Tagliavini, L., Colucci, G., Botta, A., Cavallone, P., Baglieri, L., Quaglia, G.: Wheeled mobile robots: state of the art overview and kinematic comparison among three omnidirectional locomotion strategies. Journal of intelligent & robotic systems **106**(3), 57 (2022)

[31] Isenberg, D.R., Maloziec, N., Adelman, I.: Application and benefits of using unit-quaternions for mobile robot kinematics and control. Robot Learning **2**(2), 1–24 (2025)

[32] Stefanov, N., Passenberg, C., Peer, A., Buss, M.: Design and evaluation of a haptic computer-assistant for telemanipulation tasks. IEEE Transactions on Human-Machine Systems **43**(4), 385–397 (2013)

[33] Mujica, M., Crespo, M., Benoussaad, M., Junco, S., Fourquet, J.-Y.: Robust variable admittance control for human–robot co-manipulation of objects with unknown load. Robotics and Computer-Integrated Manufacturing **79**, 102408 (2023)

[34] Chen, F., Selvaggio, M., Caldwell, D.G.: Dexterous grasping by manipulability selection for mobile manipulator with visual guidance. IEEE Transactions on Industrial Informatics **15**(2), 1202–1210 (2018)

[35] Allgeuer, P., Behnke, S.: Fused angles and the deficiencies of euler angles. In: 2018 IEEE/RSJ International Conference on Intelligent Robots and Systems (IROS), pp. 5109–5116 (2018). IEEE

[36] Schindlbeck, C., Haddadin, S.: Unified passivity-based cartesian force/impedance control for rigid and flexible joint robots via task-energy tanks. In: 2015 IEEE International Conference on Robotics and Automation (ICRA), pp. 440–447 (2015). IEEE

[37] Xing, H., Ding, L., Chen, J., Gao, H., Deng, Z.: Robotic valve turning with a wheeled mobile manipulator via hybrid passive/active compliance. Sensors **24**(17), 5559 (2024)